Hindawi
International Journal of Aerospace Engineering
Volume 2024, Article ID 8824810, 16 pages
https://doi.org/10.1155/2024/8824810

Research Article

Active Pointing Compensation of a HTS Multibeam Antenna

Xudong Wang and Pengpeng Wang

Xi'an Institute of Space Radio Technology, Xi'an 710100, China

Correspondence should be addressed to Pengpeng Wang; huohuoxjtu@163.com

Received 12 March 2023; Revised 21 January 2024; Accepted 8 February 2024; Published 29 February 2024

Academic Editor: Fangzhou Fu

Active pointing compensation of a High Throughput Satellite (HTS) multibeam antenna via microfiber composites (MFCs) is studied in this paper. Electrical-mechanical coupling analysis of MFCs is conducted to quantitatively determine driving forces and moments of MFCs attached on a carbon fiber reinforced composite (CFRP) laminate, and a positive correlation relationship is observed for driving ability versus thickness of the laminate. By different driving strategies, MFCs could act in bending mode and torsioning mode for structural deformation control, and driving efficiency of the MFCs on a multibeam antenna is studied. Thermal distortion of the antenna under a typical in orbit thermal distribution causes the reflector to rotate about y axis with an pointing error of 0.005°, active compensation is conducted, and the final compensation results show that with an optimal voltage of 432 V, pointing error of the antenna is greatly compensated, and the depointing angle is corrected to be 0.00004°.

1. Introduction

For advantages of large capacity, high efficiency, and strong flexibility, the High Throughput Satellite leads future technical trends in satellite communication and broadcasting systems [1, 2], and well-known pioneers among them are the Ka-Sat launched in 2010 and the ViaSat-1 launched in 2011 [3]. And recently, the next generation of Very High Throughput Satellites (VHTS) will be launched successively [4], such as Konnect VHS of Eutelsat and ViaSat-3 of Viasat [5, 6].

The HTS covers the target coverage with many overlapping high gain spot beams and allows a high degree of frequency reuse, which can increase the system capacity enormously, and it is clear that increasing number of the spots and bandwidth per spot will be helpful [7, 8]. With indispensable function of overlapping spot beam creation, multibeam antennas are among the key components of HTS system, and there are continually increasing demands in the need of the antennas to provide larger numbers of narrower spot beams operating over broader bandwidths [9–11]. Typically, the spot beam size is in the range of 0.45° to 0.60°; however, some recent requests for proposal have shown a demand target of 0.20° to 0.30° [12–14].

The narrower spot beam demand on the antenna also highlights the importance of accurate pointing; otherwise, system electrical performance may be greatly deteriorated. For example, a sharp reduction of 2 dB is found in a Ku band multibeam antenna as a depointing of 0.12° [15]. Usually, pointing error of the antenna consists of deployment repeatability error, alignment error of the satellite platform, assembly error of the antenna, and thermal induced error. The first three errors are constant errors which can be eliminated by in orbit calibrations. However, the thermal induced error changes with temperature distribution variation of the antenna and cannot be eliminated by in orbit calibration; thus in orbit depointing, compensation is crucial for high performance maintenance of satellite multibeam antennas [16, 17].

Multibeam antennas are usually mounted on side panels with an offset feed configuration, as depicted in Figure 1. The antenna is stowed for launch and deployed for work, and the deployed structure is in a cantilever mode, which increases the complexity of vibration control but on the other hand shows a possibility for active pointing compensation. Traditional active pointing compensation methods usually adopt pointing mechanisms to achieve a direct

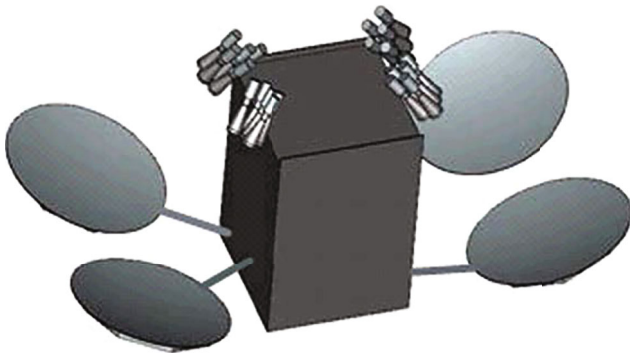

Figure 1: Multibeam antennas on a satellite platform.

pointing modification and have the benefits of high accuracy, large output, and reliable repeatability, which have been verified by enormous space applications [18–20]. However, as shown in Figure 2, they are usually large in size and heavy in weight, which may waste precious payload resources of the launchers, and propose critical requirements on the structural stiffness and strength. So, the demand for a more compact and efficient active pointing compensation method is becoming increasingly urgent.

Compared with shortages of the traditional pointing mechanisms in dimension and mass, smart materials utilize piezoelectric, electrostrictive, magnetostrictive, shape memory, and other multiphysical field coupling effects to realize active control and can be highly integrated with the main structure, and tremendous efforts have been made in their applications in space structures [21–24]. As an outstanding representative of smart materials, the macrofiber composite was firstly proposed by Langley Research Center of NASA in 1996 and was commercialized by Smart Material Corp. in 2002. By making piezoelectric ceramics fibrous and then recombines it with organic polymer matrix, the new piezoelectric composite overcomes shortcomings of traditional piezoelectric materials, such as easy to be damaged and hard to be integrated, and shows superiority in durability, flexibility, and output efficiency [25–27]. Thomas et al. investigated an analytical and finite element modeling, with experimental validation of the bending strain and deflection of an epoxy E-glass fiber composite laminate with distributed MFC actuator patches [28]. Glukhikh et al. employed built-in deformation MFC actuators to control twisting of a helicopter blade for reducing its vibration and noise [29].

So far, majority of the researches were focused on applications on beams, plates, shells, and other simple objects, and some of them were about active control of airfoils, blades, bridge cables, and similar engineering structures; however, according to the available literatures, applications of MFC on space structures especially space antennas are somewhat lacking. It may be out of the following reasons: (a) it is difficult to evaluate thermal deformation of the antennas, as rigid movements and elastic distortions of the structures are mixed together; (b) for the antennas usually made of composite materials, a precise electrical-mechanical coupling model of the MFCs and composite materials is needed.

This paper addresses active pointing compensation of a HTS multibeam antenna via microfiber composites. First, electrical-mechanical coupling analysis of the microfiber composites is conducted, and driving forces and moments of bending mode and torsioning mode are analyzed. Second, driving efficiency analysis of the MFCs on a multibeam antenna is studied. Third, thermal distortion evaluation of the antenna is given. Fourth, thermal distortion compensation of the antenna is verified. Finally, a few concluding remarks and further research suggestions are made.

2. Mechanical-Electrical Coupling Analysis

2.1. Mechanical-Electrical Model of the MFC. By different arrangements of electrodes and piezoelectric fibers, MFCs act as P1/F1 type or P2/P3 type. For P1/F1 type, the piezoelectric ceramics are polarized along the fibers, which promise a higher displacement and force output, and P1 type MFCs are usually used as extending and bending actuators while F1 type MFCs are used as torsioning actuators. MFCs of M-8857-P1 from Smart Material Corp. are shown in Figure 3, the patch is 103 mm × 64 mm with an active area of 85 × 57 mm, and the maximal operating voltage is 1500 V with an extreme displacement output of 114.75 μm and a force output of 693 N.

The inverse piezoelectric equation of MFC in material coordinate system can be listed as

$$\begin{bmatrix} \varepsilon_1 \\ \varepsilon_2 \\ \gamma_{12} \end{bmatrix} = \begin{bmatrix} \frac{1}{E_{11}} & -\frac{\mu_{12}}{E_{11}} & 0 \\ -\frac{\mu_{21}}{E_{22}} & \frac{1}{E_{22}} & 0 \\ 0 & 0 & \frac{1}{G_{12}} \end{bmatrix} \begin{bmatrix} \sigma_1 \\ \sigma_2 \\ \tau_{12} \end{bmatrix} + \begin{bmatrix} d_{11} \\ d_{12} \\ d_{16} \end{bmatrix} E, \quad (1)$$

where 1 and 2 directions are in correspondence with the longitudinal and transverse axes of the MFC and the piezoceramic fibers are polarized along 1 direction. E_{11}, E_{22}, and G_{12} refer to material elasticity modulus and shear modulus; μ_{12} and μ_{21} are the Poisson ratios; ε_1, ε_2, and γ_{12} denote the tensile strains and shear strain; σ_1, σ_2, and τ_{12} represent the tensile stresses and shear stress; and d_{11}, d_{12}, and d_{16} are piezoelectric strain constants with $d_{16} = 0$. E is electric field intensity in 1 direction.

Stresses in the MFC can be obtained as

$$\begin{bmatrix} \sigma_1 \\ \sigma_2 \\ \tau_{12} \end{bmatrix} = \frac{1}{1-\mu_{12}\mu_{21}} \begin{Bmatrix} E_{11}\varepsilon_1 + \mu_{12}E_{22}\varepsilon_2 - (d_{11}E_{11} + \mu_{12}d_{12}E_{22})E \\ \mu_{21}E_{11}\varepsilon_1 + E_{22}\varepsilon_2 - (\mu_{21}d_{11}E_{11} + d_{12}E_{22})E \\ 0 \end{Bmatrix}. \quad (2)$$

Suppose offset angle between the piezoelectric fibers and the structure global coordinate is θ, stresses in global

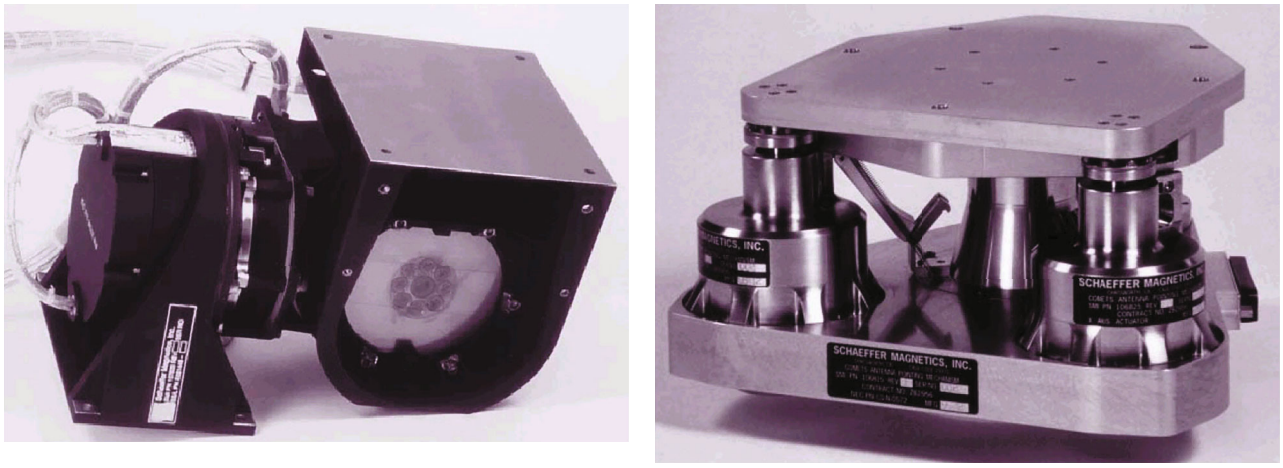

(a) (b)

Figure 2: Active pointing mechanism on INTELSAT VIIA and COMETS (4.6 kg, 230 mm × 180 mm × 170 mm and 2.97 kg, 240 mm × 230 mm × 120 mm).

Figure 3: Layout of F1 type MFCs.

coordinate can be represented by stresses in material coordinate as

$$\begin{aligned} \sigma_x &= \sigma_1 \cos^2\theta + \sigma_2 \sin^2\theta - \tau_{12} \sin 2\theta, \\ \sigma_y &= \sigma_1 \sin^2\theta + \sigma_2 \cos^2\theta + \tau_{12} \sin 2\theta, \\ \tau_{xy} &= (\sigma_1 - \sigma_2) \sin \frac{2\theta}{2} + \tau_{12} \cos 2\theta. \end{aligned} \tag{3}$$

It can be inferred from Eq. (3) that by changing the offset angle θ, the MFC could apply tensile stresses or shear stresses on structures, and the MFC is used in a bending mode or a torsioning mode.

For bending mode (P1 type MFCs), $\theta = 0^\circ$ and 1 and 2 directions are in correspondence with the x and y directions, and there exist

$$\begin{aligned} \sigma_x &= \sigma_1, \\ \sigma_y &= \sigma_2, \\ \tau_{xy} &= 0. \end{aligned} \tag{4}$$

For torsioning mode (F1 type MFCs), $\theta = 45^\circ$ and there exist

$$\begin{aligned} \sigma_x &= \frac{\sigma_1 + \sigma_2}{2}, \\ \sigma_y &= \frac{\sigma_1 + \sigma_2}{2}, \\ \tau_{xy} &= \frac{\sigma_1 - \sigma_2}{2}. \end{aligned} \tag{5}$$

Strains in the MFC and the laminate can be expressed by strains and curvatures in the neutral surface as

$$\begin{aligned} \varepsilon_x &= \varepsilon_x^0 + z\kappa_x, \\ \varepsilon_y &= \varepsilon_y^0 + z\kappa_y, \\ \gamma_{xy} &= \gamma_{xy}^0 + z\kappa_{xy}, \end{aligned} \tag{6}$$

where ε_x^0, ε_y^0, and γ_{xy}^0 refer to tensile strains and shear strain and κ_x, κ_y, and κ_{xy} denote bending curvatures and twisting curvature.

Forces and moments in the MFC lateral surfaces are given as

$$\begin{Bmatrix} F_{mx} \\ F_{my} \\ F_{mxy} \end{Bmatrix} = \int_h^{h+t} \begin{Bmatrix} b\sigma_{mx} \\ a\sigma_{my} \\ b\tau_{mxy} \end{Bmatrix} dz \begin{Bmatrix} M_{mx} \\ M_{my} \\ M_{mxy} \end{Bmatrix} = \int_h^{h+t} \begin{Bmatrix} b\sigma_{mx} \\ a\sigma_{my} \\ b\tau_{mxy} \end{Bmatrix} z dz. \tag{7}$$

Forces and moments in the laminate lateral surfaces can be obtained by the Classical Laminate Theory as

$$\begin{Bmatrix} F_{px} \\ F_{py} \\ F_{pxy} \end{Bmatrix} = \begin{bmatrix} wA_{11} & wA_{12} & wA_{16} \\ lA_{12} & lA_{22} & lA_{26} \\ wA_{16} & wA_{26} & wA_{66} \end{bmatrix} \begin{Bmatrix} \varepsilon_x^0 \\ \varepsilon_y^0 \\ \gamma_{xy}^0 \end{Bmatrix} + \begin{bmatrix} wB_{11} & wB_{12} & wB_{16} \\ lB_{12} & lB_{22} & lB_{26} \\ wB_{16} & wB_{26} & wB_{66} \end{bmatrix} \begin{Bmatrix} \kappa_x \\ \kappa_y \\ \kappa_{xy} \end{Bmatrix},$$
$$\begin{Bmatrix} M_{px} \\ M_{py} \\ M_{pxy} \end{Bmatrix} = \begin{bmatrix} wB_{11} & wB_{12} & wB_{16} \\ lB_{12} & lB_{22} & lB_{26} \\ wB_{16} & wB_{26} & wB_{66} \end{bmatrix} \begin{Bmatrix} \varepsilon_x^0 \\ \varepsilon_y^0 \\ \gamma_{xy}^0 \end{Bmatrix} + \begin{bmatrix} wD_{11} & wD_{12} & wD_{16} \\ lD_{12} & lD_{22} & lD_{26} \\ wD_{16} & wD_{26} & wD_{66} \end{bmatrix} \begin{Bmatrix} \kappa_x \\ \kappa_y \\ \kappa_{xy} \end{Bmatrix}, \tag{8}$$

where A, B, and D are stiffness matrices for extending, extending-bending coupling, and bending. A, B and D can be represented by lamina stiffness as

$$\begin{aligned} A_{ij} &= \sum_{k=1}^{n} \bar{Q}_{ij}^{k}(z_k - z_{k-1}), \\ B_{ij} &= \frac{1}{2}\sum_{k=1}^{n} \bar{Q}_{ij}^{k}\left(z_k^2 - z_{k-1}^2\right), \\ D_{ij} &= \frac{1}{3}\sum_{k=1}^{n} \bar{Q}_{ij}^{k}\left(z_k^3 - z_{k-1}^3\right), \\ & i, j = 1, 2, 6. \end{aligned} \tag{9}$$

The lamina stiffness can be further listed as

$$\begin{aligned} \bar{Q}_{11} &= Q_{11}\cos^4\theta + 2(Q_{12} + 2Q_{66})\sin^2\theta\cos^2\theta + Q_{22}\sin^4\theta, \\ \bar{Q}_{12} &= (Q_{11} + Q_{22} - 4Q_{66})\sin^2\theta\cos^2\theta + Q_{12}\left(\sin^4\theta + \cos^4\theta\right), \\ \bar{Q}_{22} &= Q_{11}\sin^4\theta + 2(Q_{12} + 2Q_{66})\sin^2\theta\cos^2\theta + Q_{22}\cos^4\theta, \\ \bar{Q}_{16} &= (Q_{11} - Q_{12} - 2Q_{66})\sin\theta\cos^3\theta + (Q_{12} - Q_{22} + 2Q_{66})\sin^3\theta\cos\theta, \\ \bar{Q}_{26} &= (Q_{11} - Q_{12} - 2Q_{66})\sin^3\theta\cos\theta + (Q_{12} - Q_{22} + 2Q_{66})\sin\theta\cos^3\theta, \\ \bar{Q}_{66} &= (Q_{11} + Q_{22} - 2Q_{12} - 2Q_{66})\sin^2\theta\cos^2\theta + Q_{66}\left(\sin^4\theta + \cos^4\theta\right). \end{aligned} \tag{10}$$

Finally, force and moment balancing at the four lateral surfaces can be expressed as

$$\begin{aligned} F_{mx} + F_{px} &= 0, \qquad M_{mx} + M_{px} = 0, \\ F_{my} + F_{py} &= 0, \qquad M_{my} + M_{py} = 0, \\ F_{mxy} + F_{pxy} &= 0, \qquad M_{mxy} + M_{pxy} = 0. \end{aligned} \tag{11}$$

2.2. Bending Mode. For bending mode, there are only tensile stresses at the MFC and the laminate lateral surfaces, as illustrated in Figure 4.

Force balancing and moment balancing relationship can be rewritten as

$$\begin{aligned} &\left[\frac{E_1 t}{1-\mu_{12}\mu_{21}} + A_{11}\right]\varepsilon_x^0 + \left[\frac{\mu_{12}E_2 t}{1-\mu_{12}\mu_{21}} + A_{12}\right]\varepsilon_y^0 \\ &\quad + \left[\frac{E_1 t(2h+t)}{2(1-\mu_{12}\mu_{21})} + B_{11}\right]\kappa_x \\ &\quad + \left[\frac{\mu_{12}E_2 t(2h+t)}{2(1-\mu_{12}\mu_{21})} + B_{12}\right]\kappa_y \\ &= \frac{t(d_{11}E_1 + \mu_{12}d_{12}E_2)}{1-\mu_{12}\mu_{21}}E, \\ &\left[\frac{\mu_{21}E_1 t}{1-\mu_{12}\mu_{21}} + A_{12}\right]\varepsilon_x^0 + \left[\frac{E_2 t}{1-\mu_{12}\mu_{21}} + A_{22}\right]\varepsilon_y^0 \\ &\quad + \left[\frac{\mu_{21}E_1 t(2h+t)}{2(1-\mu_{12}\mu_{21})} + B_{12}\right]\kappa_x \\ &\quad + \left[\frac{E_2 t(2h+t)}{2(1-\mu_{12}\mu_{21})} + B_{22}\right]\kappa_y \\ &= \frac{t(\mu_{21}d_{11}E_1 + d_{12}E_2)}{1-\mu_{12}\mu_{21}}E, \\ &\left[\frac{E_1 t(2h+t)}{2(1-\mu_{12}\mu_{21})} + B_{11}\right]\varepsilon_x^0 + \left[\frac{\mu_{12}E_2 t(2h+t)}{2(1-\mu_{12}\mu_{21})} + B_{12}\right]\varepsilon_y^0 \\ &\quad + \left[\frac{E_1 t\left(3h^2+3ht+t^2\right)}{3(1-\mu_{12}\mu_{21})} + D_{11}\right]\kappa_x \\ &\quad + \left[\frac{\mu_{12}E_2 t\left(3h^2+3ht+t^2\right)}{3(1-\mu_{12}\mu_{21})} + D_{12}\right]\kappa_y \\ &= \frac{t(2h+t)(d_{11}E_1 + \mu_{12}d_{12}E_2)}{2(1-\mu_{12}\mu_{21})}E, \\ &\left[\frac{\mu_{21}E_1 t(2h+t)}{2(1-\mu_{12}\mu_{21})} + B_{12}\right]\varepsilon_x^0 + \left[\frac{E_2 t(2h+t)}{2(1-\mu_{12}\mu_{21})} + B_{22}\right]\varepsilon_y^0 \\ &\quad + \left[\frac{\mu_{21}E_1 t\left(3h^2+3ht+t^2\right)}{3(1-\mu_{12}\mu_{21})} + D_{12}\right]\kappa_x \\ &\quad + \left[\frac{E_2 t\left(3h^2+3ht+t^2\right)}{3(1-\mu_{12}\mu_{21})} + D_{22}\right]\kappa_y \\ &= \frac{t(2h+t)(\mu_{21}d_{11}E_1 + d_{12}E_2)}{2(1-\mu_{12}\mu_{21})}E. \end{aligned} \tag{12}$$

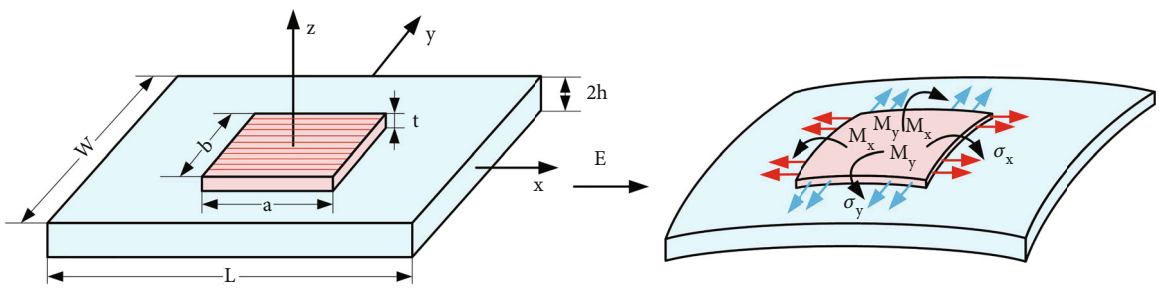

Figure 4: Bending mode of the MFCs.

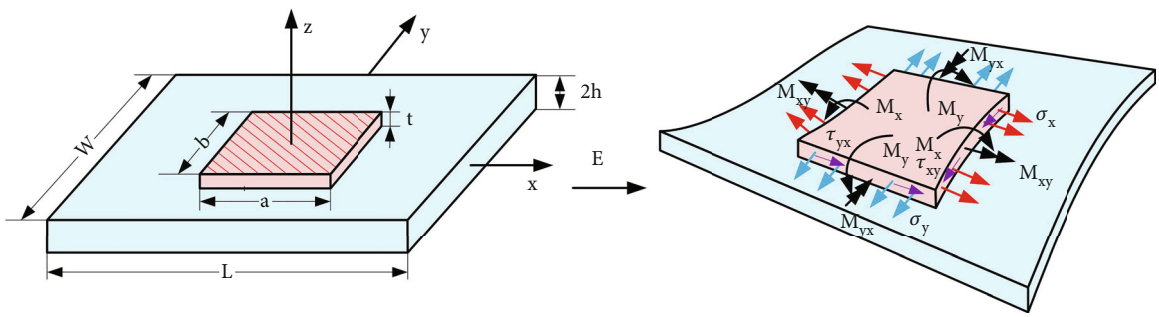

Figure 5: Torsioning mode of the MFCs.

Table 1: Geometry and material parameters of the MFCs and the laminate.

Parts	Parameters	Value
MFCs	Length a (mm)	85
	Width b (mm)	57
	Thickness t (mm)	0.30
	Elastic modulus E_{mx} (GPa)	30.336
	Elastic modulus E_{my} (GPa)	15.857
	Poisson's ratio μ_{mx}	0.31
	Poisson's ratio μ_{my}	0.16
	Piezoelectric strain constant d_{xx} (pC/N)	460
	Piezoelectric strain constant d_{xy} (pC/N)	-180
Laminate	Length l (mm)	85
	Width w (mm)	57 m
	Elastic modulus E_{px} (GPa)	180
	Elastic modulus E_{py} (GPa)	6
	Poisson's ratio μ_{px}	0.28
	Thickness h (mm)	0.80
	Number of layers n	20
	Orientation θ	$[0^\circ/45^\circ/90^\circ/-45^\circ/0^\circ/0^\circ/-45^\circ/90^\circ/45^\circ/0^\circ]_s$

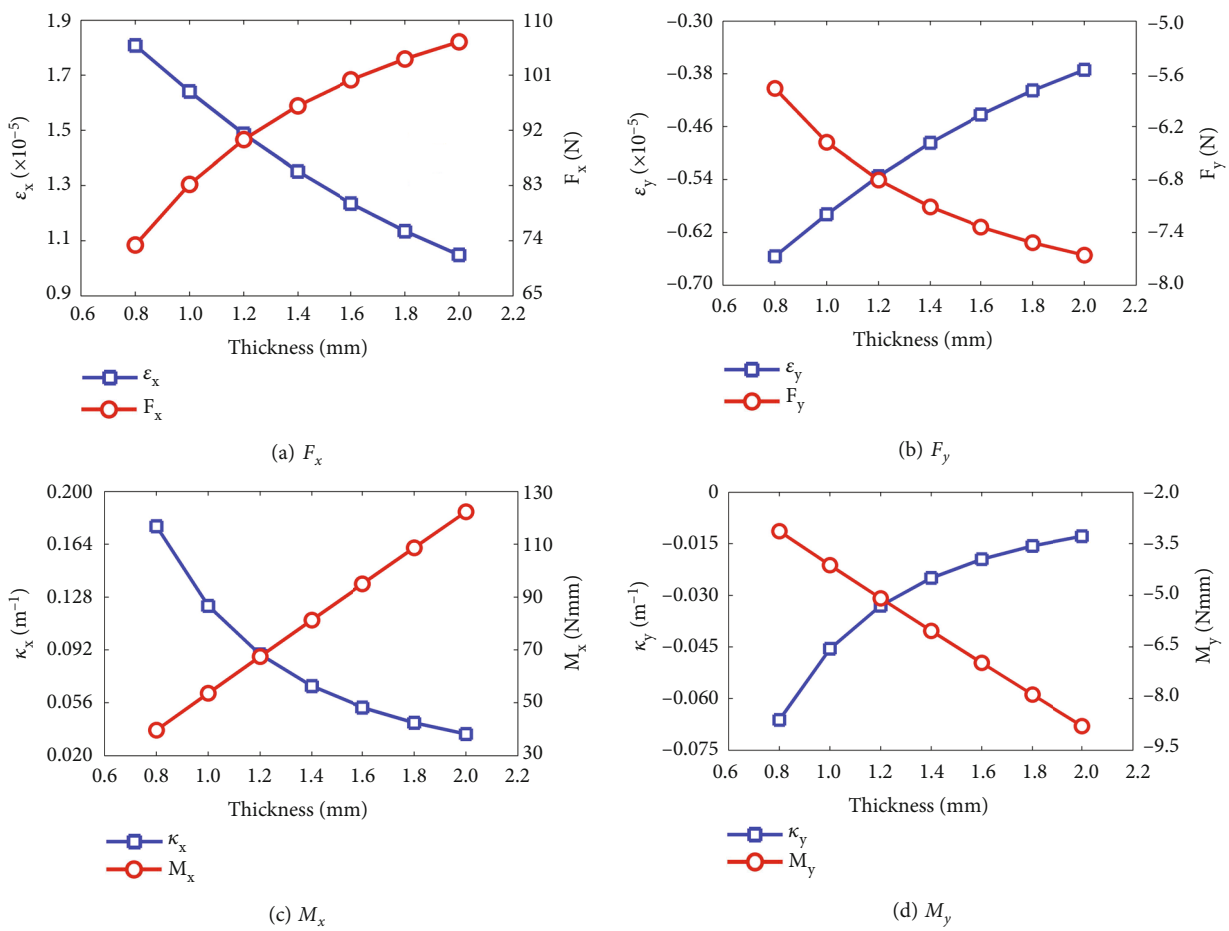

Figure 6: Driving forces and moments of bending mode.

Tensile strains ε_x^0 and ε_y^0 and bending curvatures κ_x and κ_y in neutral surface can be obtained by solving the above four equations, and the driving forces and moments applied on the laminate are given as

$$F_x = \frac{-bt}{1-\mu_{12}\mu_{21}}\left\{E_1\varepsilon_x^0 + \mu_{12}E_2\varepsilon_y^0 + \frac{E_1(2h+t)}{2}\kappa_x + \frac{\mu_{12}E_2(2h+t)}{2}\kappa_y - (d_{11}E_1 + \mu_{12}d_{12}E_2)E\right\},$$
$$F_y = \frac{-at}{1-\mu_{12}\mu_{21}}\left\{\mu_{21}E_1\varepsilon_x^0 + E_2\varepsilon_y^0 + \frac{\mu_{21}E_1(2h+t)}{2}\kappa_x + \frac{E_2(2h+t)}{2}\kappa_y - (\mu_{21}d_{11}E_1 + d_{12}E_2)E\right\},$$
$$M_x = \frac{-bt}{(1-\mu_{12}\mu_{21})}\left[\frac{E_1(2h+t)}{2}\varepsilon_x^0 + \frac{\mu_{12}E_2(2h+t)}{2}\varepsilon_y^0 + \frac{E_1(3h^2+3ht+t^2)}{3}\kappa_x + \frac{\mu_{12}E_2(3h^2+3ht+t^2)}{3}\kappa_y - \frac{(2h+t)(d_{11}E_1+\mu_{12}d_{12}E_2)}{2}E\right],$$
$$M_y = \frac{-at}{(1-\mu_{12}\mu_{21})}\left[\frac{\mu_{21}E_1(2h+t)}{2}\varepsilon_x^0 + \frac{E_2(2h+t)}{2}\varepsilon_y^0 + \frac{\mu_{21}E_1(3h^2+3ht+t^2)}{3}\kappa_x + \frac{E_2(3h^2+3ht+t^2)}{3}\kappa_y - \frac{(2h+t)(\mu_{21}d_{11}E_1+d_{12}E_2)}{2}E\right]. \tag{13}$$

2.3. Torsioning Mode. For torsioning mode, there are both tensile stresses and shear stresses at the MFC and the laminate lateral surfaces, as illustrated in Figure 5.

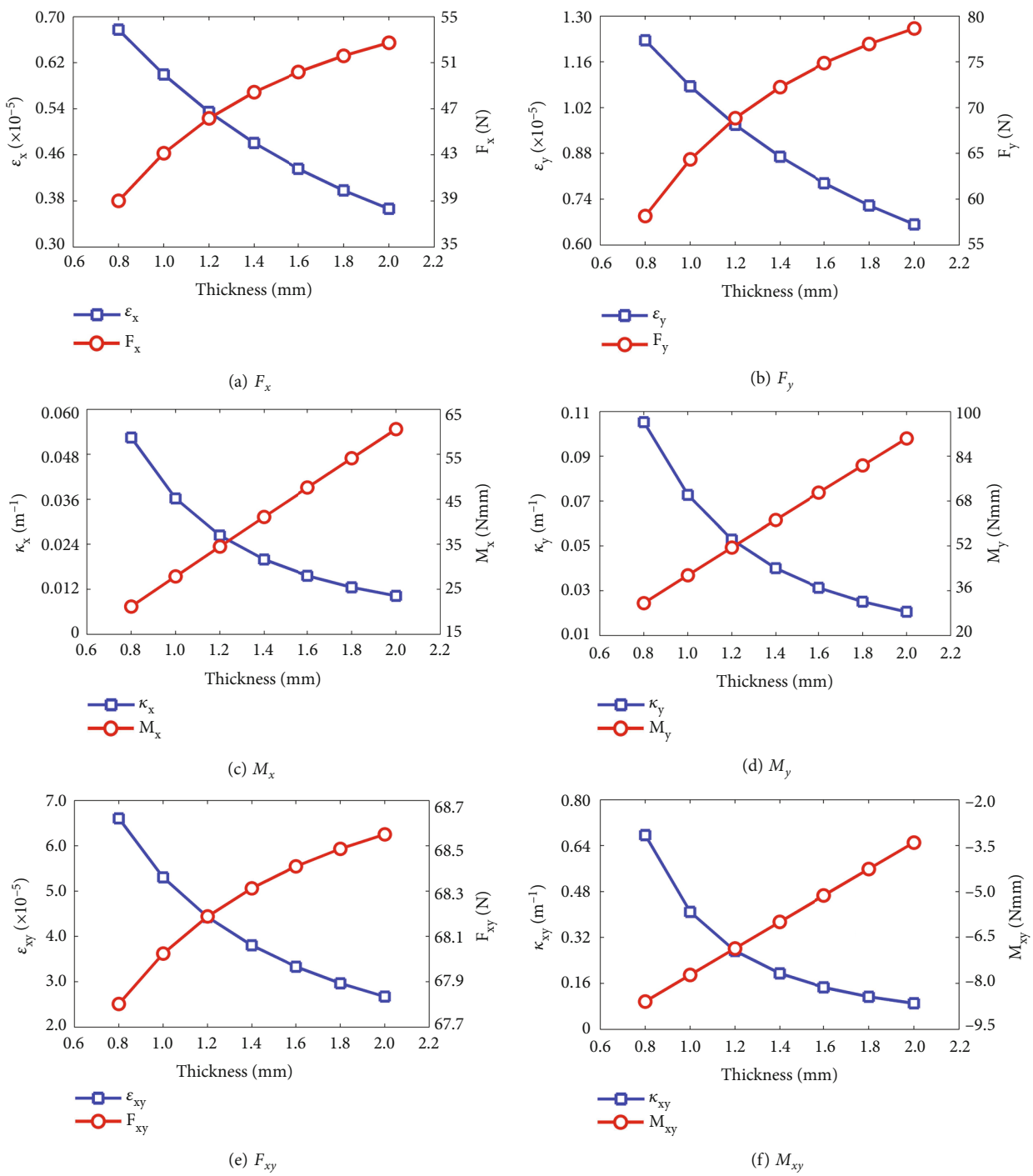

Figure 7: Driving forces and moments of torsioning mode.

Force balancing and bending moment balancing relationship can be rewritten as

$$\begin{aligned}
&\left[\frac{E_1 t(1+\mu_{21})}{1-\mu_{12}\mu_{21}}+2A_{11}\right]\varepsilon_x^0+\left[\frac{E_2 t(1+\mu_{12})}{1-\mu_{12}\mu_{21}}+2A_{12}\right]\varepsilon_y^0+[2A_{16}]\gamma_{xy}^0\\
&\quad+\left[\frac{E_1 t(2h+t)(1+\mu_{21})}{2(1-\mu_{12}\mu_{21})}+2B_{11}\right]\kappa_x\\
&\quad+\left[\frac{E_2 t(2h+t)(1+\mu_{12})}{2(1-\mu_{12}\mu_{21})}+2B_{12}\right]\kappa_y+[2B_{16}]\kappa_{xy}\\
&\quad=\frac{t[d_{11}E_1(1+\mu_{21})+d_{12}E_2(1+\mu_{12})]}{1-\mu_{12}\mu_{21}}E,
\end{aligned}$$

$$\begin{aligned}
&\left[\frac{E_1 t(1+\mu_{21})}{1-\mu_{12}\mu_{21}}+2A_{12}\right]\varepsilon_x^0+\left[\frac{E_2 t(1+\mu_{12})}{1-\mu_{12}\mu_{21}}+2A_{22}\right]\varepsilon_y^0+[2A_{26}]\gamma_{xy}^0\\
&\quad+\left[\frac{E_1 t(2h+t)(1+\mu_{21})}{2(1-\mu_{12}\mu_{21})}+2B_{12}\right]\kappa_x\\
&\quad+\left[\frac{E_2 t(2h+t)(1+\mu_{12})}{2(1-\mu_{12}\mu_{21})}+2B_{22}\right]\kappa_y+[2B_{26}]\kappa_{xy}\\
&\quad=\frac{t[d_{11}E_1(1+\mu_{21})+d_{12}E_2(1+\mu_{12})]}{1-\mu_{12}\mu_{21}}E,
\end{aligned}$$

$$\begin{aligned}
&\left[\frac{E_1 t(1-\mu_{21})}{1-\mu_{12}\mu_{21}}+2A_{16}\right]\varepsilon_x^0+\left[\frac{E_2 t(\mu_{12}-1)}{1-\mu_{12}\mu_{21}}+2A_{26}\right]\varepsilon_y^0\\
&\quad+[2A_{66}]\gamma_{xy}^0+\left[\frac{E_1 t(2h+t)(1-\mu_{21})}{2(1-\mu_{12}\mu_{21})}+2B_{16}\right]\kappa_x\\
&\quad+\left[\frac{E_2 t(2h+t)(\mu_{12}-1)}{2(1-\mu_{12}\mu_{21})}+2B_{26}\right]\kappa_y+[2B_{66}]\kappa_{xy}\\
&\quad=\left\{\frac{t[d_{11}E_1(1-\mu_{21})+d_{12}E_2(\mu_{12}-1)]}{(1-\mu_{12}\mu_{21})}\right\}E,
\end{aligned}$$

$$\begin{aligned}
&\left[\frac{E_1 t(2h+t)(1+\mu_{21})}{2(1-\mu_{12}\mu_{21})}+2B_{11}\right]\varepsilon_x^0\\
&\quad+\left[\frac{E_2 t(2h+t)(1+\mu_{12})}{2(1-\mu_{12}\mu_{21})}+2B_{12}\right]\varepsilon_y^0+[2B_{16}]\gamma_{xy}^0\\
&\quad+\left[\frac{E_1 t(3h^2+3ht+t^2)(1+\mu_{21})}{3(1-\mu_{12}\mu_{21})}+2D_{11}\right]\kappa_x\\
&\quad+\left[\frac{E_2 t(3h^2+3ht+t^2)(1+\mu_{12})}{3(1-\mu_{12}\mu_{21})}+2D_{12}\right]\kappa_y+[2D_{16}]\kappa_{xy}\\
&\quad=\left\{\frac{t(2h+t)[d_{11}E_1(1+\mu_{21})+d_{12}E_2(1+\mu_{12})]}{2(1-\mu_{12}\mu_{21})}\right\}E,
\end{aligned}$$

$$\begin{aligned}
&\left[\frac{E_1 t(2h+t)(1+\mu_{21})}{2(1-\mu_{12}\mu_{21})}+2B_{12}\right]\varepsilon_x^0\\
&\quad+\left[\frac{E_2 t(2h+t)(1+\mu_{12})}{2(1-\mu_{12}\mu_{21})}+2B_{22}\right]\varepsilon_y^0+[2B_{26}]\gamma_{xy}^0\\
&\quad+\left[\frac{E_1 t(3h^2+3ht+t^2)(1+\mu_{21})}{3(1-\mu_{12}\mu_{21})}+2D_{12}\right]\kappa_x\\
&\quad+\left[\frac{E_2 t(3h^2+3ht+t^2)(1+\mu_{12})}{3(1-\mu_{12}\mu_{21})}+2D_{22}\right]\kappa_y+[2D_{26}]\kappa_{xy}\\
&\quad=\left\{\frac{t(2h+t)[d_{11}E_1(1+\mu_{21})+d_{12}E_2(1+\mu_{12})]}{2(1-\mu_{12}\mu_{21})}\right\}E,
\end{aligned}$$

Table 2: Driving forces and moments of bending mode and torsioning mode.

Driving forces and moments		Bending mode	Torsioning mode
Driving forces (N)	F_x	100.3	50.2
	F_y	-7.3	74.8
	F_{xy}	0	68.4
	F_{xy}	0	102.1
Driving moments (Nmm)	M_x	95.1	47.9
	M_y	-7.2	71.4
	M_{xy}	0	65.3
	M_{yx}	0	97.4

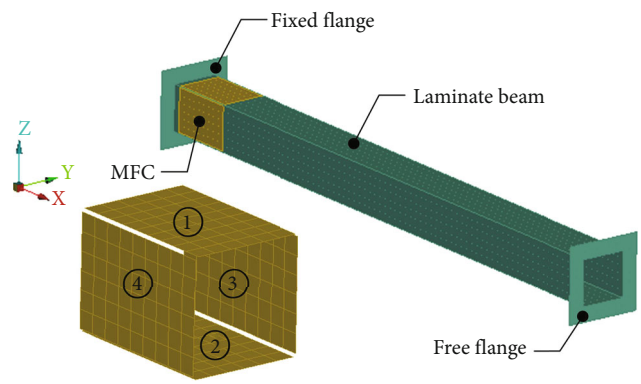

Figure 8: Layout of the antenna.

Table 3: Driving strategies of the MFCs.

Driving outputs	Deformation directions	MFC_1	MFC_2	MFC_3	MFC_4
Extending	Elongation along X	+1	+1	+1	+1
	Contraction along X	-1	-1	-1	-1
Bending	Rotation about Y	+1	-1	0	0
	Rotation about Z	0	0	-1	+1
Torsioning	Rotation about X	-1	+1	0	0
	Rotation about X	0	0	+1	-1

$$\begin{aligned}
&\left[\frac{E_1 t(2h+t)(1-\mu_{21})}{2(1-\mu_{12}\mu_{21})}+2B_{16}\right]\varepsilon_x^0\\
&\quad+\left[\frac{E_2 t(2h+t)(\mu_{12}-1)}{2(1-\mu_{12}\mu_{21})}+2B_{26}\right]\varepsilon_y^0+[2B_{66}]\gamma_{xy}^0\\
&\quad+\left[\frac{E_1 t(3h^2+3ht+t^2)(1-\mu_{21})}{3(1-\mu_{12}\mu_{21})}+2D_{16}\right]\kappa_x\\
&\quad+\left[\frac{E_2 t(3h^2+3ht+t^2)(\mu_{12}-1)}{3(1-\mu_{12}\mu_{21})}+2D_{26}\right]\kappa_y+[2D_{66}]\kappa_{xy}\\
&\quad=\left\{\frac{t(2h+t)[d_{11}E_1(1-\mu_{21})+d_{12}E_2(\mu_{12}-1)]}{2(1-\mu_{12}\mu_{21})}\right\}E.
\end{aligned}\tag{14}$$

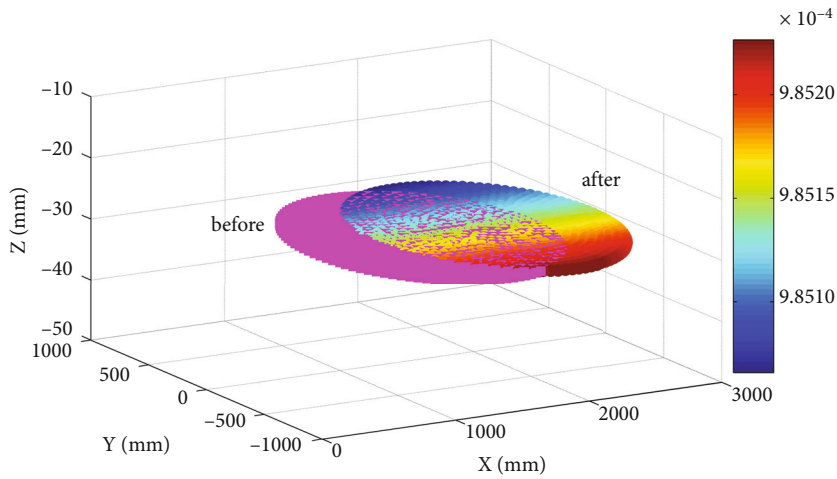

(a) Elongation along X

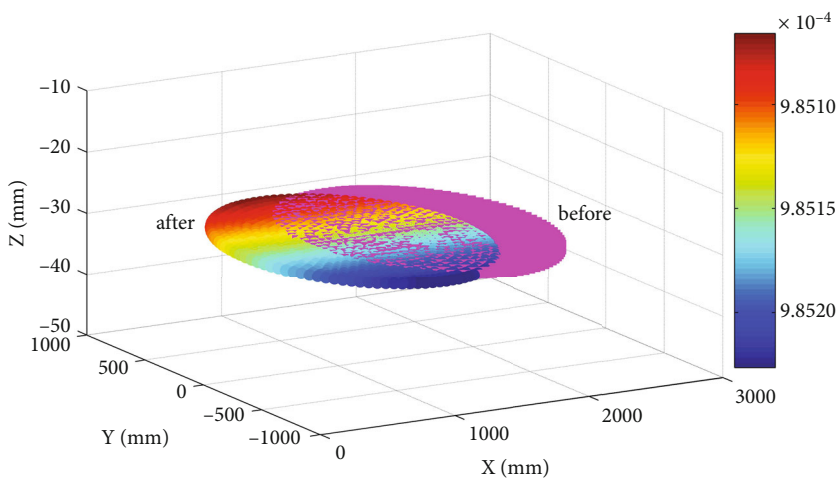

(b) Contraction along X

Figure 9: Extending mode.

Similarly, tensile strains ε_x^0 and ε_y^0, and shear strain γ_{xy}^0, bending curvatures κ_x and κ_y, and twisting curvature κ_{xy} can be obtained by solving the above six equations, and the driving forces and moments applied on the laminate are given as

$$F_x = \frac{-bt}{2(1-\mu_{12}\mu_{21})}\left\{E_1(1+\mu_{21})\varepsilon_x^0 + E_2(1+\mu_{12})\varepsilon_y^0 + \frac{(2h+t)}{2}E_1(1+\mu_{21})\kappa_x + \frac{(2h+t)}{2}E_2(1+\mu_{12})\kappa_y - [d_{11}E_1(1+\mu_{21}) + d_{12}E_2(1+\mu_{12})]E\right\},$$

$$F_y = \frac{-at}{2(1-\mu_{12}\mu_{21})}\left\{E_1(1+\mu_{21})\varepsilon_x^0 + E_2(1+\mu_{12})\varepsilon_y^0 + \frac{(2h+t)}{2}E_1(1+\mu_{21})\kappa_x + \frac{(2h+t)}{2}E_2(1+\mu_{12})\kappa_y - [d_{11}E_1(1+\mu_{21}) + d_{12}E_2(1+\mu_{12})]E\right\},$$

$$F_{xy} = \frac{-bt}{2(1-\mu_{12}\mu_{21})}\left\{E_1(1-\mu_{21})\varepsilon_x^0 + E_2(\mu_{12}-1)\varepsilon_y^0 + \frac{(2h+t)}{2}E_1(1-\mu_{21})\kappa_x + \frac{(2h+t)}{2}E_2(\mu_{12}-1)\kappa_y - [d_{11}E_1(1-\mu_{21}) + d_{12}E_2(\mu_{12}-1)]E\right\},$$

$$F_{yx} = \frac{-at}{2(1-\mu_{12}\mu_{21})}\left\{E_1(1-\mu_{21})\varepsilon_x^0 + E_2(\mu_{12}-1)\varepsilon_y^0 + \frac{(2h+t)}{2}E_1(1-\mu_{21})\kappa_x + \frac{(2h+t)}{2}E_2(\mu_{12}-1)\kappa_y - [d_{11}E_1(1-\mu_{21}) + d_{12}E_2(\mu_{12}-1)]E\right\},$$

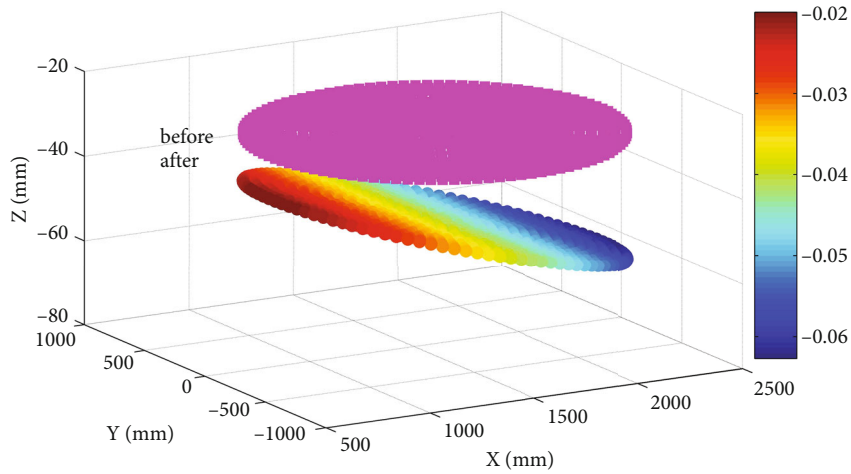

(a) Rotation about Y

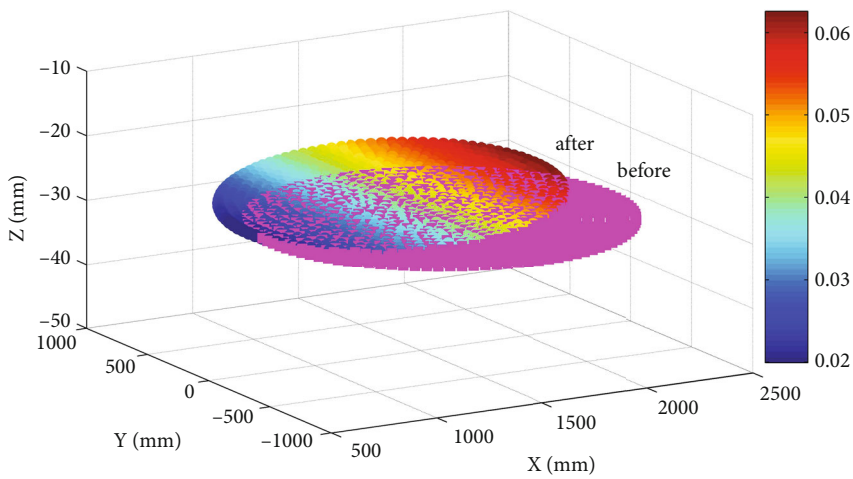

(b) Rotation about Z

Figure 10: Bending mode.

$$
\begin{aligned}
M_x = {} & \frac{-bt}{2(1-\mu_{12}\mu_{21})}\left\{\frac{(2h+t)}{2}E_1(1+\mu_{21})\varepsilon_x^0 + \frac{(2h+t)}{2}E_2(1+\mu_{12})\varepsilon_y^0\right. \\
& + \frac{(3h^2+3ht+t^2)}{3}E_1(1+\mu_{21})\kappa_x \\
& + \frac{(3h^2+3ht+t^2)}{3}E_2(1+\mu_{12})\kappa_y \\
& \left. - \frac{(2h+t)}{2}[d_{11}E_1(1+\mu_{21}) + d_{12}E_2(1+\mu_{12})]E\right\}, \\
M_{xy} = {} & \frac{-bt}{2(1-\mu_{12}\mu_{21})}\left\{\frac{(2h+t)}{2}E_1(1-\mu_{21})\varepsilon_x^0 + \frac{(2h+t)}{2}E_2(\mu_{12}-1)\varepsilon_y^0\right. \\
& + \frac{(3h^2+3ht+t^2)}{3}E_1(1-\mu_{21})\kappa_x \\
& + \frac{(3h^2+3ht+t^2)}{3}E_2(\mu_{12}-1)\kappa_y \\
& \left. - \frac{(2h+t)}{2}[d_{11}E_1(1-\mu_{21}) + d_{12}E_2(\mu_{12}-1)]E\right\}, \\
M_y = {} & \frac{-at}{2(1-\mu_{12}\mu_{21})}\left\{\frac{(2h+t)}{2}E_1(1+\mu_{21})\varepsilon_x^0 + \frac{(2h+t)}{2}E_2(1+\mu_{12})\varepsilon_y^0\right. \\
& + \frac{(3h^2+3ht+t^2)}{3}E_1(1+\mu_{21})\kappa_x \\
& + \frac{(3h^2+3ht+t^2)}{3}E_2(1+\mu_{12})\kappa_y \\
& \left. - \frac{(2h+t)}{2}[d_{11}E_1(1+\mu_{21}) + d_{12}E_2(1+\mu_{12})]E\right\}, \\
M_{yx} = {} & \frac{-at}{2(1-\mu_{12}\mu_{21})}\left\{\frac{(2h+t)}{2}E_1(1-\mu_{21})\varepsilon_x^0 + \frac{(2h+t)}{2}E_2(\mu_{12}-1)\varepsilon_y^0\right. \\
& + \frac{(3h^2+3ht+t^2)}{3}E_1(1-\mu_{21})\kappa_x \\
& + \frac{(3h^2+3ht+t^2)}{3}E_2(\mu_{12}-1)\kappa_y \\
& \left. - \frac{(2h+t)}{2}[d_{11}E_1(1-\mu_{21}) + d_{12}E_2(\mu_{12}-1)]E\right\}.
\end{aligned}
\tag{15}
$$

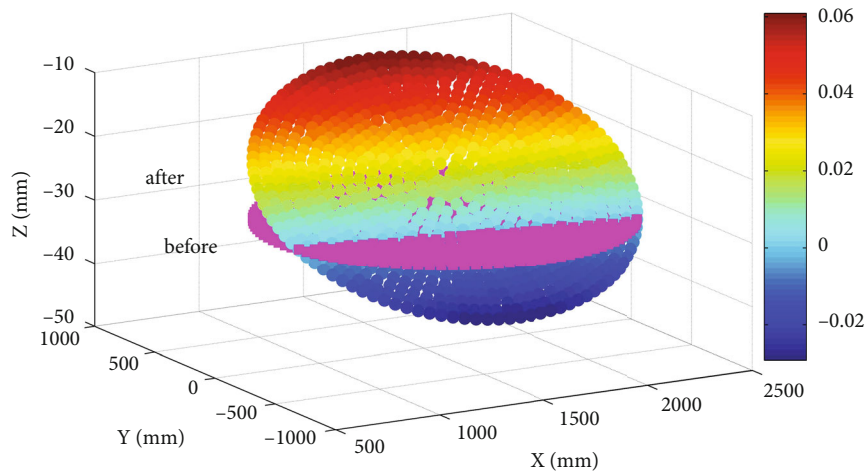

(a) Rotation about X

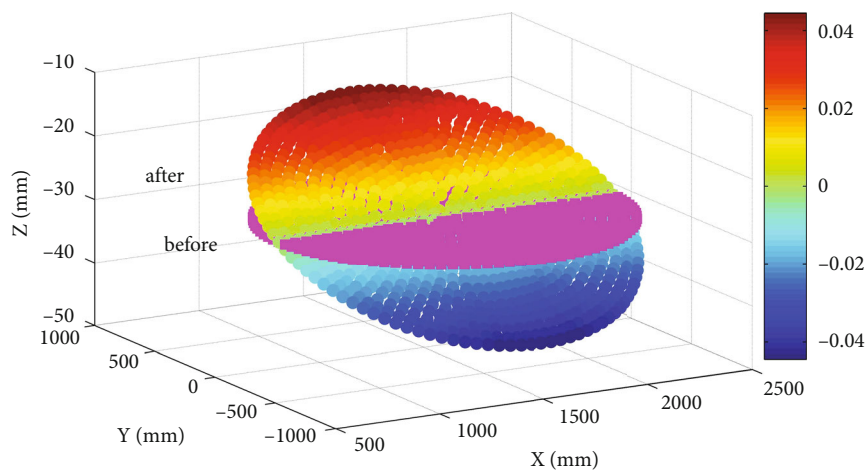

(b) Rotation about X

Figure 11: Torsioning mode.

2.4. Driving Force and Moment Analysis. Strains in the MFC are composed of elastic strain result from the structural deformation and piezoelectric strains induced by the electric field. So driving forces and moments of the MFC are not only determined by geometry and material parameters of itself, such as the dimension $a \times b \times t$, the tensile elastic modulus E_1 and E_2, and the Poisson ratios μ_{12} and μ_{21}, but also affected by these of the laminate. Geometry and material parameters of the MFC and the laminate are listed in Table 1.

Variations of driving forces and moments over different laminate thicknesses are shown in Figures 6 and 7, the driving forces and moments increase with the laminate thickness, and it is observed that the relationship is linear for driving moments, but nonlinear for driving forces.

For MFCs and laminate with parameters listed in Table 1, driving forces and moments of the bending mode and torsioning mode are summarized in Table 2.

3. Control Efficiency Analysis on the Antenna

3.1. Configuration of the Antenna. As depicted in Figure 8, a multibeam antenna mainly consists of a fixed flange, a free flange, a laminate beam, and a reflector. The laminate beam is made of a combination of twenty layers of CFRP prepregs, and the layer angle orientation is $[0^\circ/45^\circ/90^\circ/\text{-}45^\circ/0^\circ/0^\circ/\text{-}45^\circ/90^\circ/45^\circ/0^\circ]_s$. The reflector is 1600 mm in diameter and is composed of sixteen CFRP prepreg layers with a layer angle arrangement of $[0^\circ/45^\circ/\text{-}45^\circ/90^\circ]_4$. The reflector is connected with the laminate beam through six bolts at the free flange, and the laminate beam is mounted on the satellite platform at the fixed flange interface. As influences of solar radiation, earth reflection, and shadowing, thermal distribution of the reflector changes periodically in orbit, and thermal distortion of the structure will cause pointing deviation of the antenna and degenerate the system performance. Four MFCs are bonded on the four lateral surfaces of the laminate beam, it is expected that depointing of the antenna can be compensated by active control of the MFCs, and by different deformation demands, the MFCs could be P1 type or F1 type.

3.2. Driving Strategies of the MFCs. By different driving strategies, the four MFCs could be combined to apply extension forces, bending moments, and torsioning moments on the laminate beam, as listed in Table 3.

Table 4: Driving efficiencies of the MFCs for different driving strategies.

Driving outputs	Deformation directions		Translations and rotations ($\times 10^{-3}$)					
			TX (mm)	T (mm)	TZ (mm)	RX (°)	RY (°)	RZ (°)
Extending	Elongation along X		0.991	0.001	-0.042	0.001	-0.001	-0.001
	Contraction along X		-0.991	-0.001	0.042	-0.001	0.001	0.001
Bending	Rotation about Y		0.004	-0.005	1.523	0.002	1.531	0.001
	Rotation about Z		0.001	-1.482	0.053	-0.001	0.001	1.528
Torsioning	Rotation about X		-0.011	-0.291	-0.48	3.173	-0.584	0.021
	Rotation about X		0.003	0.754	0.048	3.186	0.001	-0.604

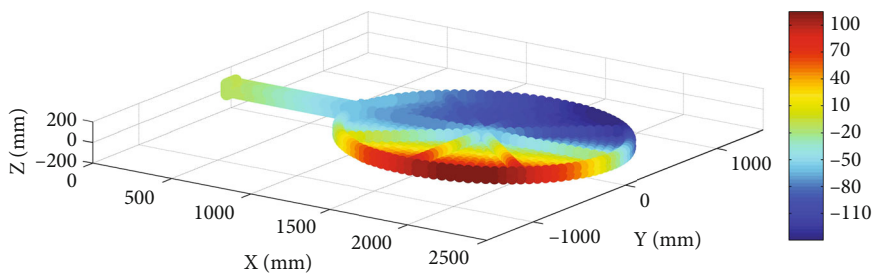

Figure 12: A typical thermal distribution map of the antenna.

Movements of the reflector under the above driving strategies are shown in Figures 9–11. For extending, four MFCs are driven with the same voltage, and the antenna deforms along the deploy beam. For bending and torsioning, two MFCs at opposite surfaces are driven with voltage inputs that are same in amplitude but opposite in polarity, and opposite normal strains or shear strains arise at the beam lateral surfaces, which cause the deploy beam to bend or turn around.

3.3. Driving Efficiencies of the MFCs. Surface distortions of the reflector are composed of rigid translations and rotations of the reflector which refer to its rigid movements and elastic deformation of the reflector which changes its shape contour, and it is the so-called "best fit paraboloid." Suppose there are uniformly distributed targets on the reflector, and surface contour of the reflector can be represented by space coordinates of the targets. Rigid translation and rotation of the reflector, which is induced by driving forces and moments of the MFCs, can be obtained by solving the optimization problem listed below.

$$\begin{aligned} &\text{Find} \quad \boldsymbol{T}(tx, ty, tz, \alpha, \beta, \gamma) = \begin{bmatrix} \boldsymbol{R} & \boldsymbol{D} \\ \boldsymbol{0} & \boldsymbol{I} \end{bmatrix} \\ &\min \quad \mathrm{RMS}\{\boldsymbol{B} - \boldsymbol{R}(\boldsymbol{A} - \boldsymbol{D})\} \\ &\text{s.t.} tx \in [tx_{\min}, tx_{\max}], ty \in [ty_{\min}, ty_{\max}], tz \in [tz_{\min}, tz_{\max}] \\ &\alpha \in [\alpha_{\min}, \alpha_{\max}], \beta \in [\beta_{\min}, \beta_{\max}], \gamma \in [\gamma_{\min}, \gamma_{\max}], \end{aligned} \tag{16}$$

where $\mathbf{A}$ and $\mathbf{B}$ are space coordinate matrices of the reflector before and after control; tx, ty, and tz refer to rigid translations of the reflector along x, y, and z axes; and α, β, and γ denote rigid rotations about x, y, and z axes.

By the evaluation method proposed above, driving efficiencies of the MFCs for different driving strategies can be summarized in Table 4.

As a voltage vector E is applied on the MFCs, the antenna deforms with a displacement vector $\mathbf{U}_m$, and the mechanical-electrical relationship can be simplified as

$$\mathbf{U}_m = \mathbf{C}_m E, \tag{17}$$

where $\mathbf{C}_m$ is defined as mechanical-electrical coefficient matrix between the output deformation and the input voltage.

4. Thermal Distortion Evaluation of the Antenna

By influences of solar radiation, earth reflection, and shadowing, temperature of the antenna changes periodically in an orbit cycle. A typical thermal distribution map is illustrated in Figure 12, and the antenna has to resist a maximal temperature of 100°C and a minimal temperature of -110°C; for the deploy beam, the temperature varies gradually along

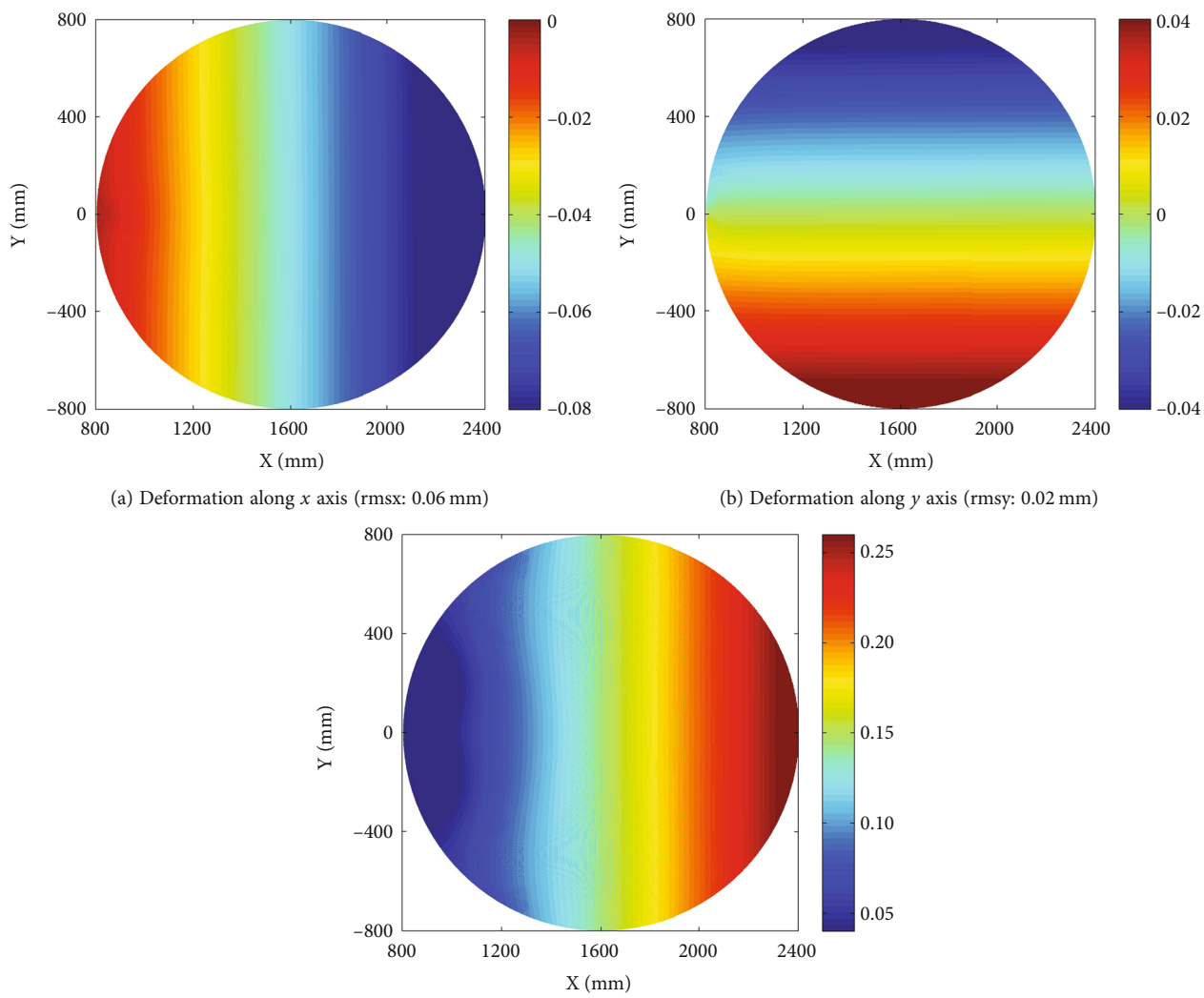

(a) Deformation along x axis (rmsx: 0.06 mm)

(b) Deformation along y axis (rmsy: 0.02 mm)

(c) Deformation along z axis (rmsz: 0.16 mm)

Figure 13: Thermal deformations of the reflector.

the x axis; however, for the reflector, there is a manifest temperature gradient along the y axis.

The unbalanced thermal distribution applies a thermal load on the structure and cause deformation of the reflector which can be determined as

$$\mathbf{K}\mathbf{U}_t = \mathbf{F}_t, \tag{18}$$

where $\mathbf{K}$, $\mathbf{U}_t$, and $\mathbf{F}_t$ refer to the global stiffness matrix, displacement vector, and thermal load vector of the antenna.

Deformations of the reflector along x, y, and z axes are shown in Figure 13, and root mean square errors of the reflector in x, y, and z are 0.06 mm, 0.02 mm, and 0.16 mm. An obvious rotation about the y axis is illustrated in Figure 13(c), and as deformation along z axis could cause phase variation of the electromagnetic waves and deteriorate the electrical performance, a pointing compensation should be considered.

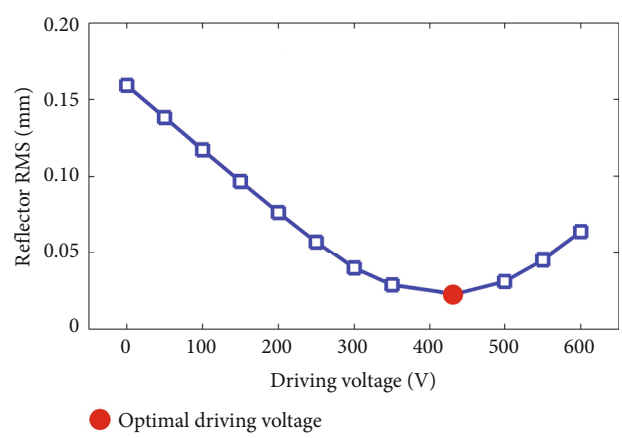

Figure 14: Reflector RMS versus driving voltages.

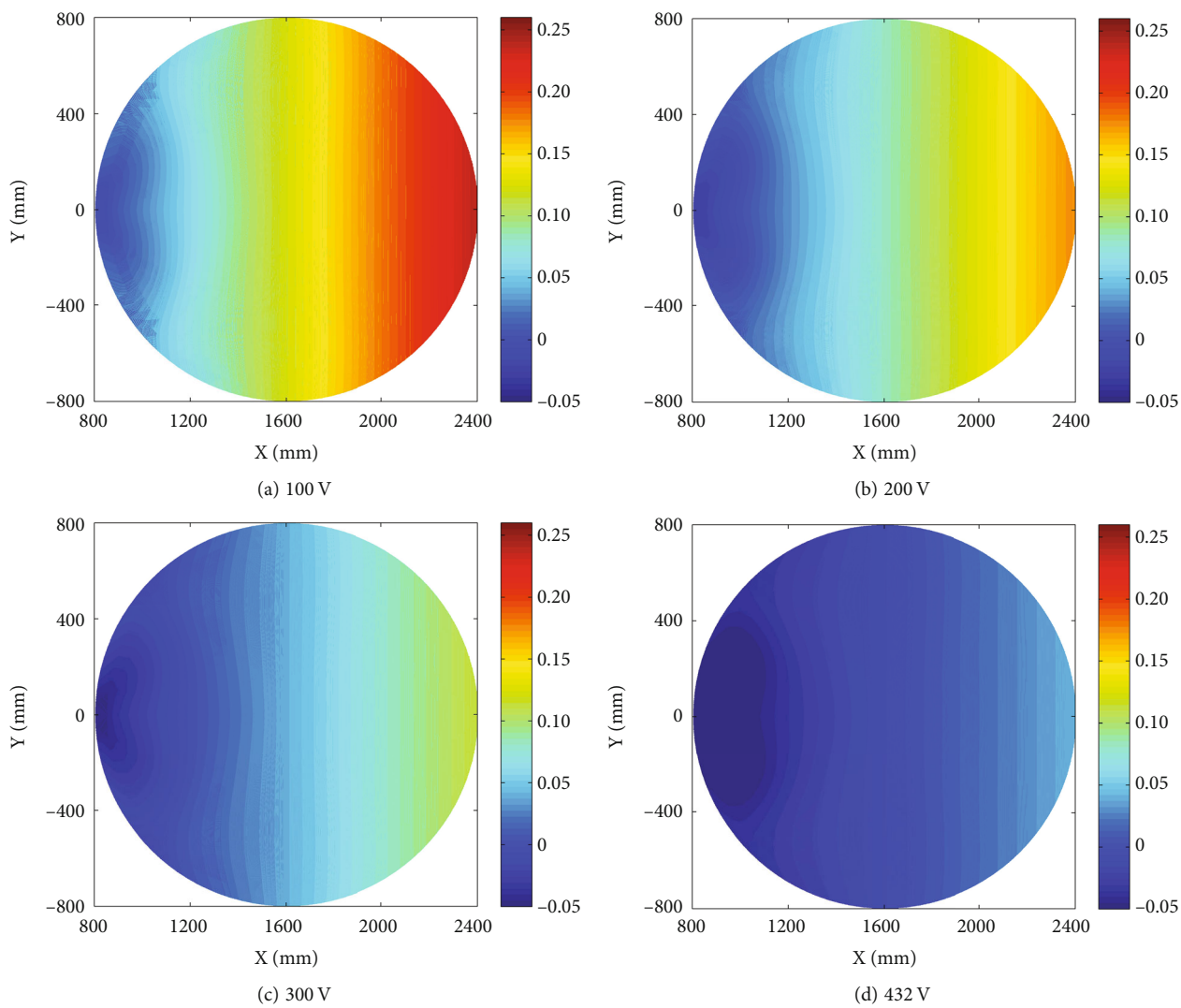

Figure 15: Thermal deformations of the reflector under different driving voltages.

5. Pointing Error Compensation of the Antenna

Displacement vector of the antenna under thermal load is given as

$$\mathbf{U}_t = \mathbf{K}^{-1}\mathbf{F}_t. \tag{19}$$

Also, displacement vector induced by the MFC driving forces and moments is

$$\mathbf{U}_m = \mathbf{C}_m E. \tag{20}$$

The final deformation of the antenna is sum of the above two displacement vectors as

$$\mathbf{U} = \mathbf{U}_t + \mathbf{U}_m = \mathbf{K}^{-1}\mathbf{F}_t + \mathbf{C}_m E. \tag{21}$$

Deformation of the reflector in z direction can be obtained by coordinate transformation as

$$\mathbf{Z} = \mathbf{QP}\left(\mathbf{K}^{-1}\mathbf{F}_t + \mathbf{C}_m E\right), \tag{22}$$

where $\mathbf{P}$ is the location matrix of the reflector targets and $\mathbf{Q}$ is the transform matrix for z coordinate.

Finally, root mean square of the reflector in z coordinate is

$$\mathrm{RMS}^2 = \frac{1}{n}\mathbf{Z}^T\mathbf{Z} = \frac{1}{n}\left(\mathbf{K}^{-1}\mathbf{F}_t + \mathbf{C}_m E\right)^T \mathbf{P}^T\mathbf{Q}^T\mathbf{QP}\left(\mathbf{K}^{-1}\mathbf{F}_t + \mathbf{C}_m E\right). \tag{23}$$

Then, pointing compensation of the antenna can be simplified to be a quadratic programming problem as

$$\begin{gathered} \min_E \frac{1}{2} E\mathbf{H}E + \mathbf{f}^T E \\ \text{s.t.} E_{\min} \le E \le E_{\max} \\ \mathbf{H} = \mathbf{C}_m^T\mathbf{P}^T\mathbf{Q}^T\mathbf{QPC}_m \\ \mathbf{f} = \mathbf{F}_t^T\mathbf{K}^{-T}\mathbf{P}^T\mathbf{Q}^T\mathbf{QPC}_m + \mathbf{C}_m^T\mathbf{P}^T\mathbf{Q}^T\mathbf{QPK}^{-1}\mathbf{F}_t. \end{gathered} \tag{24}$$

By solving the above quadratic programming problem, the optimal control voltage which can furthest compensate thermal induced rotation of the reflector could be found as illustrated in Figure 14. Root mean square of the reflector reaches its minimum 0.02 mm with a driving voltage of 432 V.

Surface distortions of the reflector at different control voltages are illustrated in Figure 15, and as the driving voltage increases from 0 V to 432 V, rotation of the reflector is corrected gradually. At 0 V driving voltage, root mean square of the reflector is 0.16 mm with a rotation angle 0.005° about y axis, while at 432 V, the rotation angle is corrected to be 0.00004° and the corresponding surface distortion is 0.02 mm.

6. Conclusions

In this paper, active pointing compensation of a HTS multibeam antenna via microfiber composites is studied, and the main contributions of this study are summarized as follows:

(a) Electrical-mechanical coupling analysis of the MFCs is conducted, and by solving mechanical balance relationships, driving forces and moments of MFCs on a CFRP laminate is studied, and it is observed that the active loads increase with thickness of the controlled structure

(b) The MFCs show promising driving efficiencies for both bending control and torsioning control; by changing driving strategies, the MFCs could drive extending, bending, and torsioning deformations of the controlled structure

(c) An obvious depointing of the reflector is caused by unbalanced in orbit thermal load, with a pointing error of 0.005° and a surface root mean square of 0.16 mm. Active pointing compensation of the reflector is conducted by applying an optimal voltage of 432 V on the MFCs, and the control results are satisfying with a residual pointing error of 0.00004° and a surface root mean square of 0.02 mm

However, until now, all the study is conducted with a single-layer MFC configuration, and the driving voltage 432 V after optimization is close to voltage threshold of the material, which is -500 V ~1500 V, so further study may focus on pointing compensation with multiple layer MFCs and other possible methods to reduce the driving voltages.

In addition, the harsh space environment of the antenna in orbit poses various limitations on the use of MFC, especially the complex thermal environment and space irradiation effects. It should be acknowledged that currently, the vast majority of MFC applications are mainly concentrated in ground environments, and a small number of space applications such as solar wings and space boom are still in the simulation stage. The publicly reported engineering applications are only seen in the ST-123 Rigidizable Inflatable Get-Away-Special Experiment in 2008. The applicable temperature range given in the MFC user manual is -35°C to +130°C, while for space antennas, the temperature range can usually reach -150°C to +150°C. Therefore, additional thermal control measures need to be taken, such as coating multiple layers of thermal control and sticking film heaters, to ensure the appropriate working temperature of the MFC. Meanwhile, the effects of space ultraviolet radiation and material creep are issues that need to be carefully considered. Therefore, the adaptability of MFC to the spatial environment will be an important direction for future research.

Data Availability

The data used to support the findings of this study are available from the corresponding author upon request.

Conflicts of Interest

The authors declare that there is no conflict of interest regarding the publication of this paper.

Acknowledgments

This work was supported by the National Natural Science Foundation of China (grant no. U1537213).

References

[1] H. Fenech, S. Amos, A. Tomatis, and V. Soumpholphakdy, "High throughput satellite systems: an analytical approach," *IEEE Transactions on Aerospace and Electronic Systems*, vol. 51, no. 1, pp. 192–202, 2015.

[2] Y. Vasavada, R. Gopal, C. Ravishankar, G. Zakaria, and N. BenAmmar, "Architectures for next generation high throughput satellite systems," *International Journal of Satellite Communications and Networking*, vol. 34, no. 4, pp. 523–546, 2016.

[3] H. Fenech, A. Tomatis, S. Amos, V. Soumpholphakdy, and J. L. Serrano Merino, "Eutelsat HTS systems," *International Journal of Satellite Communications and Networking*, vol. 34, no. 4, pp. 503–521, 2016.

[4] R. D. Gaudenzi, P. Angeletti, D. Petrolati, and E. Re, "Future technologies for very high throughput satellite systems," *International Journal of Satellite Communications and Networking*, vol. 38, no. 2, pp. 141–161, 2020.

[5] https://www.thalesgroup.com/en/worldwide/space/press-release/eutelsat-konnect-vhts-communications-satellite-successfully-launched.

[6] A. Aguilar, P. Butler, J. Collins, M. Guerster, and E. F. Crawley, "Tradespace exploration of the next generation communication satellites," in *AIAA SciTech Forum and Exposition*, San Diego, USA, 2019.

[7] Z. Katona, C. Kourogiorgas, A. D. Panagopoulos, and N. Jeannin, "Capacity analysis of high-throughput satellite links for earth observation missions," *International Journal of Satellite Communications and Networking*, vol. 33, no. 5, pp. 429–449, 2015.

[8] A. J. Roumeliotis, C. I. Kourogiorgas, and A. D. Panagopoulos, "Optimal dynamic capacity allocation for high throughput satellite communications systems," *IEEE Wireless Communications Letters*, vol. 8, no. 2, pp. 596–599, 2019.

[9] E. Martinez-de-Rioja, D. Martinez-de-Rioja, J. A. Encinar et al., "Advanced multibeam antenna configurations based on reflectarrays: providing multispot coverage with a smaller

number of apertures for satellite communications in the K and Ka bands," *IEEE Antennas and Propagation Magazine*, vol. 61, no. 5, pp. 77–86, 2019.

[10] P. Bosshard, J. Lafond, F. Dubos et al., "Thales Alenia Space HTS/V-HTS multiple beam antennas sub-systems on the right track," in *10th European Conference on Antennas and Propagation*, Davos, Switzerland, 2016.

[11] H. Fenech, S. Amos, A. Tomatis, J. S. Merino, and V. Soumpholphakdy, "The many guises of HTS antennas," in *8th European Conference on Antennas and Propagation*, Hague, Netherlands, 2014.

[12] E. Amyotte, Y. Demers, L. Hildebrand, S. Richard, and S. Mousseau, "A review of multibeam antenna solutions and their applications," in *8th European Conference on Antennas and Propagation*, Hague, Netherlands, 2014.

[13] M. Schneider, C. Hartwanger, and H. Wolf, "Antennas for multiple spot beam satellites," *CEAS Space Journal*, vol. 2, no. 1-4, pp. 59–66, 2011.

[14] D. Martinez-de-Rioja, E. Martinez-de-Rioja, J. A. Encinar, R. Florencio, and G. Toso, "Reflectarray to generate four adjacent beams per feed for multispot satellite antennas," *IEEE Transactions on Antennas and Propagation*, vol. 67, no. 2, pp. 1265–1269, 2019.

[15] P. P. Wang, X. D. Wang, and W. J. Jiang, "Failure analysis of a high precision deployable reflector in TED test," *Engineering Failure Analysis*, vol. 111, article 104482, 2020.

[16] B. D. You, J. M. Wen, and J. Chen, "Pointing control of satellite antenna considering dynamic error of flexible-joint," in *10th IEEE International Conference on Control and Automation*, Hangzhou, China, 2013.

[17] P. P. Wang, F. Wang, T. Shi, and W. Wang, "Thermal distortion compensation of a high precision umbrella antenna," *Journal of Physics: Conference Series*, vol. 916, article 012051, 2017.

[18] X. Li, X. L. Ding, and G. S. Chirikjian, "Analysis of a mechanism with redundant drive for antenna pointing," *Proceedings of the Institution of Mechanical Engineers, Part G: Journal of Aerospace Engineering*, vol. 231, no. 2, pp. 229–239, 2017.

[19] M. Pfeiffer, R. Purschke, and J. Harder, "Design, construction and testing of a 2 degree of freedom Ka-band antenna pointing mechanism," in *60th International Astronautical Congress*, Daejeon, Korea, 2009.

[20] R. Purschke and A. Hoehn, "Design and characterization of an antenna pointing mechanism for on-orbit servicing missions," in *2013 IEEE Aerospace Conference*, Big Sky, MT, USA, 2013.

[21] K. Culler, "Active isolation and pointing using flextensional piezoelectric actuators," in *39th AIAA Aerospace Sciences Meeting and Exhibit*, Reno, NV, USA, 2001.

[22] S. B. Shao, Y. Shao, S. Y. Song, M. L. Xu, and X. F. Ma, "Structure and controller design of a piezo-driven orientation stage for space antenna pointing," *Mechanical Systems and Signal Processing*, vol. 138, no. 1, article 106525, 2020.

[23] S. Kalra, B. Bhattacharya, and B. S. Munjal, "Design of shape memory alloy actuated intelligent parabolic antenna for space applications," *Smart Materials and Structure*, vol. 26, no. 9, article 095015, 2017.

[24] J. L. Fanson, "On the use of electrostrictive actuators in recovering the optical performance of the Hubble space telescope," in *Proceedings of the MRS Symposium*, Boston, MA, USA, 1994.

[25] Z. Y. An, M. L. Xu, Y. J. Luo, and C. S. Wu, "Active vibration control for a large annular flexible structure via a macro-fiber composite strain sensor and voice coil actuator," *International Journal of Applied Mechanics*, vol. 7, no. 4, article 1550066, 2015.

[26] E. Fleurent-Wilson, T. E. Pollock, W. J. Su, D. Warrier, and A. Salehian, "Wrinkle localization in membrane structures patched with macro-fiber composite actuators: inflatable space antenna applications," *Journal of Intelligent Material Systems and Structures*, vol. 25, no. 15, pp. 1978–2009, 2014.

[27] C. R. Bowen, R. Butler, R. Jervis, H. A. Kim, and A. I. T. Salo, "Morphing and shape control using unsymmetrical composites," *Journal of Intelligent Material Systems and Structures*, vol. 18, no. 1, pp. 89–98, 2007.

[28] P. R. Thomas, A. C. B. Calzada, and K. Gilmour, "Modeling of macro fiber composite actuated laminate plates and aerofoils," *Journal of Intelligent Material Systems and Structures*, vol. 31, no. 4, pp. 525–549, 2020.

[29] S. Glukhikh, E. Barkanov, A. Kovalev et al., "Design of helicopter rotor blades with actuators made of a piezomacrofiber composite," *Mechanics of Composite Materials*, vol. 44, no. 1, pp. 57–64, 2008.